PAPER • **OPEN ACCESS**

Optimizing quantum reflection of Bose–Einstein condensates with angle of incidence

To cite this article: H A Musyayyadah *et al* 2025 *Phys. Scr.* **100** 015414

Physica Scripta

PAPER

Optimizing quantum reflection of Bose–Einstein condensates with angle of incidence

H A Musyayyadah[1], M N A Halif[1,*], A Ripai[2] and Z Abdullah[2]

[1] Institute of Engineering Mathematics, Universiti Malaysia Perlis (UNIMAP) Pauh Putra Campus, Arau, Perlis, 02600, Malaysia
[2] Theoretical Physics Laboratory, Department of Physics, Faculty of Mathematics and Natural Science, Universitas Andalas, Padang 25163, Indonesia
[*] Author to whom any correspondence should be addressed.

E-mail: m.azzaurahanifah@gmail.com **and** m.nazri@unimap.edu.my

Keywords: angle of incidence, Bose–Einstein condensates, quantum reflection, saturation effect, silicon surface

OPEN ACCESS

RECEIVED
7 August 2024

REVISED
4 December 2024

ACCEPTED FOR PUBLICATION
12 December 2024

PUBLISHED
27 December 2024

Abstract

We investigated the effect of the angle of incidence on the quantum reflection of Bose–Einstein condensates (BECs) from regions with rapid potential variations. The reflection process was examined for both isotropic and anisotropic 2D disk-shaped BECs. In both cases, the angle of incidence was found to play a crucial role during reflection, inducing non-uniform atom-surface interactions and thus manipulating severe disruptions on the atomic cloud in the low incident velocity regime. In this scenario, the angle of incidence minimizes or even eliminates disruptions or fragmentation of the atomic cloud, especially for incidence angles far from the normal incidence direction. Consequently, anomalous reflectivity or saturation effects, which have been challenging in previous studies, can be effectively addressed and controlled. These findings provide new insights into optimizing the quantum reflection of BECs from a solid surface, particularly regarding the enhancement of the reflection probability of BECs from a planar silicon surface, which, since their first experiments, have not been maximized due to saturation effects.

1. Introduction

Twenty years ago, Shimizu [1] pioneered quantum reflection (QR) experiments on solid surfaces using metastable neon atoms, demonstrating that the reflection probability R increases as incident velocity v_x decreases, consistent with single atom theory [2, 3]. Observing QR on a solid surface is inherently challenging and requires atoms with extremely low energy to reach the surface, approximately $\sim k_B \times 10\text{nK}$ [4–7], which is much lower than the incident energy needed for QR observation on a liquid surface, i.e., $\sim k_B \times 10\text{mK}$ [8, 9], where k_B is the Boltzmann constant. This configuration indicates that achieving high reflectivity in QR experiments on a solid surface requires a very low incident velocity v_x. High reflectivity occurs under the condition $\phi(k) = (1/k^2)dk/dr \sim d\lambda/dr \gg 1$ [1, 10], where the local wavenumber is denoted as $k = 2\pi/\lambda$, depending on the de Broglie wavelength, λ, and r is the normal distance between the atom and the surface. Thus, an ultracold atomic gas system with a large de Broglie wavelength λ is considered highly effective for observing QR on a solid surface, providing an excellent platform for studying QR with significant flexibility in controlling atomic motion [10].

Recent studies on QR using ultracold atoms, particularly Bose–Einstein condensates (BECs), have generated significant interest due to their potential practical applications in confining ultracold atoms [10–23]. QR experiments with BECs on planar silicon (Si) surfaces, however, are still relatively unexplored, with the MIT group's work being a notable exception. Their experiments revealed anomalous reflectivity, or the so-called saturation effect, at low v_x [7]. Theoretical work by Scott *et al* [24] attributed this effect to the role of interatomic interactions, particularly the mean-field energy E_g in driving dynamical excitations such as solitons and vortex rings, which lead to condensate fragmentation and a subsequent decrease in reflection probability R at low v_x regime. Further exploration confirmed that the saturation effect in QR BECs became apparent when the mean-

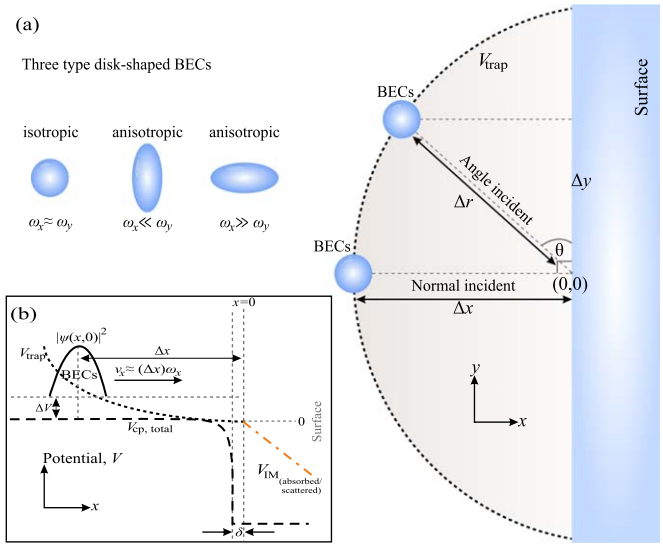

Figure 1. (a) Schematic representation of QR BECs from regions of rapid potential variations based on the angle of incidence θ. BECs are positioned at a distance Δx from the surface in normal incidence. θ is then adjusted such that BECs accelerate toward the minimum trap at (0,0) and undergo QR. QR is considered for isotropic and anisotropic disk-shaped BECs. Meanwhile, (b) illustrates the Casimir–Polder (CP) potential $V_{CP}(x)$ as a model of Si surface.

field energy dominated the incident kinetic energy, $E_g \gg E_k$ [25]. Despite these findings, enhancing the reflection probability R in QR experiments remains a challenge, particularly due to the saturation effect observed at low v_x. Previous theoretical or experimental studies [7, 16, 24–31] have primarily focused on altering surface geometry, shape, and dimensions to influence E_g and mitigate the saturation effect. For example, Pasquini *et al* [11] carved pillar structures on the solid surface to reduce atom-surface interactions and enhance QR BECs containing N ^{23}Na atoms up to 70%. However, the saturation effect remains an unresolved issue in the low v_x regime, especially when interatomic interactions are significant. Thus, achieving maximal enhancement of R has not been attained.

In this study, we propose a novel approach to optimizing QR in BECs by manipulating the angle of incidence θ, an aspect that has not been thoroughly explored in previous theoretical or experimental studies. We found that by carefully adjusting the incident angle, we can manipulate the atom-surface interactions, thereby reducing condensate fragmentation and enhancing the reflection probability R. Our work primarily investigates quasi-2D ^{23}Na BECs under Casimir–Polder (CP) potential influence, as a model of Si surface, with a detailed analysis of the disruption dynamics and the role of incident angle in modulating the observed QR behavior.

This paper presents our findings on QR in BECs with varying angles of incidence θ. In section 2, we describe our theoretical model, which uses the mean-field approach [32, 33], yielding the well-known Gross–Pitaevskii equation (GPE), where interatomic interactions are described by a nonlinear term related to the s-wave scattering length a and the condensate density n_0. We consider the BECs in a two-dimensional (2D) harmonic trap undergoing QR from regions with rapid potential variations. We perform QR simulations using the 4th-order Runge-Kutta (4RK) method, focusing on both isotropic and anisotropic condensates. Section 3 discusses our simulation results, highlighting the effect of incident angle on QR and the disruption of the condensate. Finally, we summarize our findings in section 4, underscoring the implications of our work for future experimental investigations and potential applications in atomic optical devices.

2. Model

2.1. Ilustrative description

Developing the approaches of Scott *et al* [24] and Halif [25], we model QR ^{23}Na BECs from a planar Si surface based on the incidence angle θ in a 2D system. The model illustration is presented in figure 1(a). We primarily consider BECs containing a large number of atoms N of ^{23}Na (to increase interatomic interactions) in a harmonic trap $V_{trap}(x,\ y) = m/2(\omega_x^2 x^2 + \omega_y^2 y^2)$ with strong confinement in the transverse z-direction. Here, $m = 3.81 \times 10^{-26}$ kg is the atomic mass of ^{23}Na, while ω_x and ω_y are the respective trap frequencies in the x- and y-directions. QR based on θ is modeled for three distinct BECs with different numbers of atoms N, denoted as BECs A-C, with data provided in table 1. Unlike previous studies [24, 25], in addition to the isotropic case, we also consider each QR for anisotropic disk-shaped BECs. In the isotropic case, the 2D disk-shaped BECs are

Table 1. The data for ^{23}Na BECs A-C, showing the number of atoms N, chemical potential μ_{2D}, peak density n_0, and TF radius $R_{TF;x}$, i.e., the radius of the atom cloud in the x-direction [*Note: directly computed from the model under consideration*].

BECs	N	μ_{2D}(J)	n_0(m^{-2})	$R_{TF;x;2D}$(μm)
A	1×10^4	1.0×10^{-32}	5.2×10^{12}	35
B	1×10^5	3.2×10^{-32}	1.6×10^{13}	62
C	3×10^5	5.5×10^{-32}	2.8×10^{13}	82

defined by the trap frequency configuration $(\omega_x, \omega_y, \omega_z) = 2\pi \times (3.3, 3.3, 100)$ Hz, where $\omega_x \approx \omega_y$. Meanwhile, for anisotropic 2D disk-shaped BECs, they are elongated in the x-direction when $\omega_x \ll \omega_y$ with the configuration $(\omega_x, \omega_y, \omega_z) = 2\pi \times (3.3, 6.6, 100)$ Hz. The 2D disk-shaped BECs are also elongated in the y-direction with the configuration $(\omega_x, \omega_y, \omega_z) = 2\pi \times (6.6, 3.3, 100)$ Hz or when $\omega_x \gg \omega_y$. In this study, for the isotropic case, we have adjusted the trap frequency values in line with previous theoretical and experimental studies of QR ^{23}Na BECs at normal incidence [7, 24, 25], while for the anisotropic case, the values were set specifically for simulation purposes.

At normal incidence, QR of interacting quasi-2D BECs occurs at $\theta = 90^\circ$. In this scenario, at time $t = 0$ ms, we displace the ^{23}Na BECs at a distance Δx along the x-direction from the surface. Consequently, they accelerate towards the region with rapid potential energy variation, reach the point of minimum potential energy at (0, 0), and then undergo reflection. This mechanism is akin to displacing the trap by a distance Δx from the surface [7, 24]. However, our procedure has technically simplified the computational grid minimization. For better understanding, we have complemented the illustration with a snapshot of the QR BECs model along the x-direction, as shown in figure 1(b). In this study, the angle of incidence θ is formed between the center of mass of the BECs and the potential minimum trap at the point (0, 0). Thus, when $\theta = 0^\circ$, ^{23}Na BECs are perfectly aligned with the surface at $x = 0$. This situation is undesirable for any reflection scenario, including QR, primarily because atom-surface interactions occur from the outset, causing severe disruptions to the atomic cloud throughout the process. To avoid this, we limit $\theta \in (0^\circ, 90^\circ]$. Setting the angle of incidence θ is similar to displacing the BECs by a distance $\Delta r = \sqrt{\Delta x^2 + \Delta y^2}$ from the potential minimum point. However, we prefer to refer to the values of the angle of incidence θ for practical purposes.

2.2. Reflection scenario and potential model

In this study, we consider QR of interacting quasi-2D ^{23}Na BECs under the Casimir–Polder (CP) potential V_{CP} in figure 1(b), as the model for the Si surface [24], whose form is specified later. There are two crucial parameters in the implementation of the atom-surface potential. First, a small offset (cut-off) δ, is introduced to prevent the attractive CP potential from varying too rapidly near the surface, as shown by the black dashed line in $V_{CP}(x)$ in figure 1(b). Second, the imaginary potential, V_{im} [orange dashed line in figure 1(b)], is employed to model the absorption of waves transmitted through the surface. This is crucial to prevent transmitted waves from reaching the grid walls [24, 25].

The total potential energy of each ^{23}Na atom (mass m) in the BECs is given by $V_T(x, y) = V_{CP}(x) + V_{trap}(x, y)$. In this situation, BECs are entirely trapped in a harmonic potential, while the CP potential affects the BECs according to $V_{CP}(x) = -C_4/x^3(x + 3\lambda_a/2\pi^2)$ for $x < \delta$ [figure 1(b)], where $C_4 = 9.1 \times 10^{-56}$ Jm^4 and $\lambda_a = 590$ nm is the effective atomic transition wavelength [24, 34]. For $x \geqslant \delta$, $V_{CP}(x) := V_{CP}(\delta) - iV_{im}(x + \delta)$, with $\delta = 0.15$μm, $V_{im} = 1.6 \times 10^{-26}$ J, and $V_{CP}(\delta) \approx -10^{-29}$ J [24].

2.3. Equation, solution, and techniques

We determined the dynamics of the interacting quasi-2D ^{23}Na BECs using the 4th-order Runge-Kutta (4RK) method [25, 35–37] to solve the time-dependent Gross–Pitaevskii equation (GPE) [38, 39]:

$$i\hbar\frac{\partial\psi}{\partial t} = \left[-\frac{\hbar^2}{2m}\nabla^2 + V_T(x, y) + \frac{4\pi\hbar^2 a}{m}N|\psi|^2\right]\psi, \tag{1}$$

where ∇^2 is the Laplacian in Cartesian coordinates, and $a = 2.8$ nm is the s-wave scattering length. In the 2D system, the interaction constant $g = 4\pi\hbar^2 a/m$ becomes g_{2D}, whose value is specified later. For sufficiently large N (indicating strong interatomic interactions), the static ground state of the 2D ^{23}Na BECs can be described by the Thomas-Fermi (TF) limit [40], yielding the solution:

$$\psi_{\mathrm{TF}}(x,\,y) = \mathbb{R}\left(\sqrt{n_0\left[1 - \frac{(x^2 + y^2)}{R_{\mathrm{TF}}^2}\right]}\right), \tag{2}$$

where $n_0 = \sqrt{m\omega_r^2/(\pi g_{2\mathrm{D}})}$ is the 2D condensate peak density and $R_{\mathrm{TF}} = (4g_{2\mathrm{D}}/(\pi m\omega_r^2))^{1/4}$ is the TF radius of the 2D ^{23}Na BECs. In this context, $\omega_r = \sqrt{\omega_x\omega_y}$ is the average trapping frequency. The interaction strength is given by $g_{2\mathrm{D}} = \sqrt{8\pi}\,\hbar^2 a/(ma_z)$, where $a_z = \sqrt{\hbar/m\omega_z}$ is the confined oscillation length in z-direction. Setting the ground state solution (4) as the initial atomic wave packet and simulating the GPE (1) based on the angle of incidence θ, we observe QR of interacting quasi-2D ^{23}Na BECs from a planar Si surface. Specifically, at $\theta = 90^\circ$ and $t = 0$ mm/s, we displace the initial atomic wave packet by a distance $\Delta x = 77$ μm along the x-direction from the surface. This value corresponds to a low incident velocity $v_x \approx \omega_x\Delta x = 1.6$ mm/s when the wave packet reaches regions with rapid potential variation, i.e., V_{CP}. To obtain other velocities along the x-direction up to 3.0 mm/s, we multiply the initial wave function by a phase factor $\phi(x) = \exp(ikx)$, where $k = mv_i/\hbar$ is the wave number corresponding to the initial velocity $v_i^2 = v_f^2 - (\Delta x\omega_x)^2$, and v_f refers to the final velocity, i.e., the velocity when the atom reaches the surface [25]. As mentioned in Sub-section 2.1, we can adjust the trap displacement to obtain specific incident velocities [7, 24]. However, once again, our technical procedures have facilitated minimizing computational grids.

We determined the reflection probability R as the integral of the probability density of the wave function over $x < 0$: $R = \int_{-\infty}^{0} |\psi(x,\,y,\,t_s)|^2\,dxdy$, where t_s is the time at the end of the simulation after the reflection process is completed. For practical purposes, we only compute R with respect to the incident velocity along the x-direction, v_x. This is specifically done to compare the results with previous theoretical and experimental studies under normal incidence [7, 24, 25]. Since V_{im} has provided absorption of waves transmitted through the surface [see Sub-section 2.2], we decided to focus solely on the reflection probability R. Following the same technical procedure, we observe the QR of interacting quasi-2D ^{23}Na BECs for various angles of incidence $\theta \in [15^\circ, 90^\circ]$. These incidence angles have been adjusted so that atom-surface interaction do not occur initially (before collision). Once again, we perform QR simulations for three distinct interacting quasi-2D ^{23}Na BECs [table 1], each for both isotropic and anisotropic cases.

3. Results and discussion

3.1. Initial groundstate of BECs

Figure 2(a)-(i) shows the initial ground-state atomic density profiles of isotropic and anisotropic 2D disk-shaped BECs in the x-y plane. For both isotropic and anisotropic cases, stronger interatomic interactions (larger N values) result in a more significant atomic cloud size for each 2D disk-shaped BEC. Simultaneously, BECs with larger atomic cloud sizes exhibit higher peak densities, as indicated by all BEC C in figure 2(c), (f), and (i) in this case. The conversion from dimensionless scale units in the figures is given by $\tilde{n}i = nia_x^2/N$, where i refers to BECs A-C, n_i is the peak density, a_x is the oscillation length in the x-direction, and N is the number of atoms. The significance of peak density along with the increase in atomic cloud size for larger N is a common phenomenon and can be easily verified through manual calculations related to the relationship between n_0 and the TF radius in the x-direction, $R_{\mathrm{TF};x}$, as provided in table 1. For deeper understanding, figure 2(g)-(i) shows that anisotropic quasi-2D disk-shaped BECs elongated in the x-direction exhibit a larger atomic cloud size and higher peak density compared to isotropic BECs [figures 2(a)-(c)]. Conversely, when the anisotropic quasi-2D disk-shaped BECs are elongated in the y-direction, figures 2(d)-(f) shows smaller peak densities and atomic cloud sizes, being the smallest among the two previous cases. This configuration corresponds to the trap frequency settings we previously established [see section 2.1], with its consequences on QR described later. The results of our study on the initial ground-state atomic density [figures 2(a)-(i)] are consistent with and confirm previous theoretical studies [24, 25] and experimental studies [7, 11] for ^{23}Na BECs at normal incidence. Additionally, this study provides new insights into the characteristics of anisotropic ground-state BECs and their impact on QR, which will be discussed further later.

3.2. Quantum reflection at normal incidence

After understanding the ground state of each BEC, both for isotropic and anisotropic cases, we then investigated the QR of quasi-2D ^{23}Na BECs interacting with a planar Si surface at normal incidence, $\theta = 90^\circ$. Figure 3(a)-(c) depicts images of the 2D disk-shaped BECs (isotropic and anisotropic) before ($t = 0$ ms), during ($t = 41$ ms), and after ($t = 63$ ms) the collision with the planar Si surface (CP potential). Following Scott *et al* [24], strong interatomic interactions are an important feature during QR and crucial to study in enhancing QR at low incident velocities v_x [see section 1]. Therefore, this phenomenon was first observed for BEC C, which has strong interatomic interactions, at low incident velocity ($v_x = 1.0$ mm/s) and high incident velocity ($v_x = 3.0$mm/s). The corresponding incident velocity values refer to the displacement of BEC C by $\Delta x = 48$ μm and $\Delta x = 145$ μm

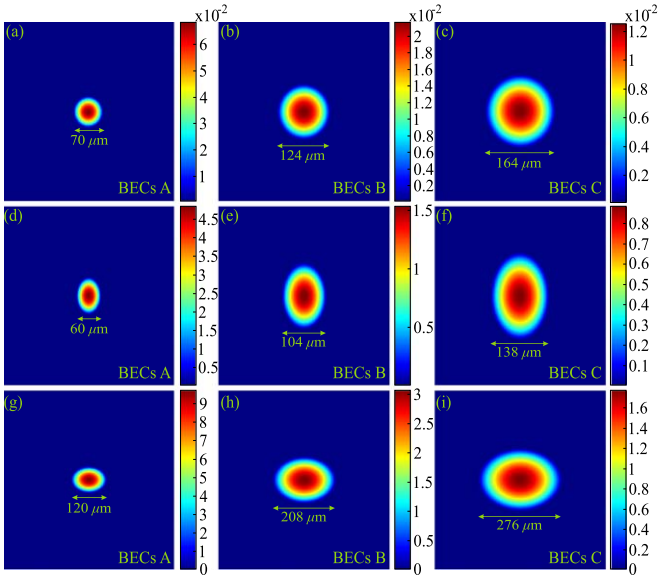

Figure 2. The initial ground state atom density of ^{23}Na BECs in the x-y plane, respectively for the three 2D disk-shaped BECs: BECs A (First column), BECs B (Second column), and BECs C (Third column), with corresponding parameters in table 1. (a)-(c) isotropic disk-shaped BECs, (d)-(f) anisotropic disk-shaped BECs elongated in the y-direction, and (g)-(i) anisotropic disk-shaped BECs elongated in the x-direction. Horizontal arrows indicate the size of BECs along the longitudinal x-direction, i.e., l_x. Inset scale bars show the scale of the dimensionless unit of density $\tilde{n}_i$, where i = A, B, C is the index of BECs A-C.

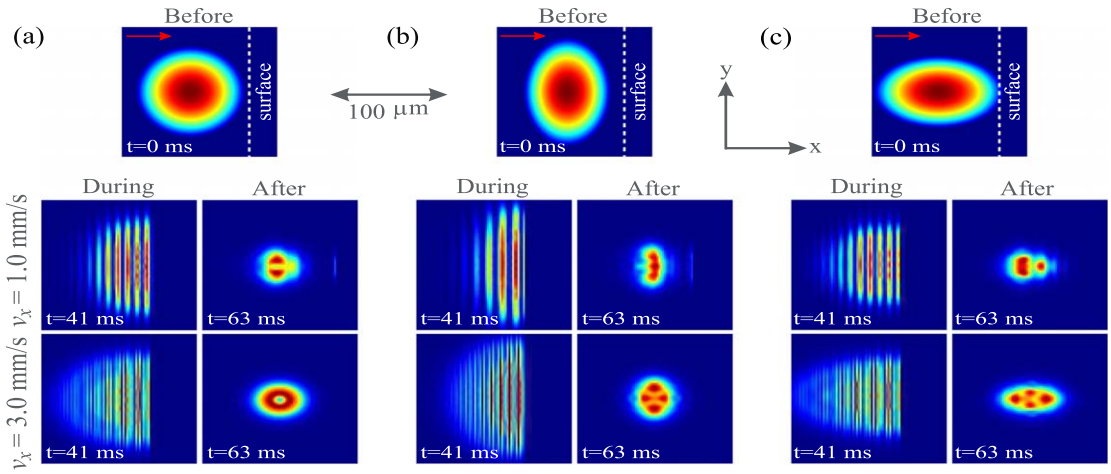

Figure 3. (dark red = high density) in the $x-y$ plane showing QR of isotropic (a), anisotropic elongated in y-direction (b), and anisotropic elongated in x-direction (c) ^{23}Na BECs C from a planar Si surface in normal incidence, $\theta = 90^0$, with incident speed $v_x = 1.0$ mm/s (upper plots) and $v_x = 3.0$ mm/s (lower plots). From left to right represent BECs before ($t = 0$ ms), during ($t = 41$ ms), and after collision ($t = 63$ ms). The red arrows indicate the direction of BECs that undergo QR.

from the planar Si surface [see Subsection 2.3]. Based on figure 3(a)-(c), we can clearly observe the significant disruption of the atomic cloud during QR of the isotropic and anisotropic 2D disk-shaped BEC C, especially at $v_x = 1.0$ mm/s, which is more pronounced compared to $v_x = 3.0$ mm/s. The significant disruption of the atomic cloud at low v_x during QR is fundamentally supported by the strong interatomic interactions (larger N values) exhibited by BEC C in this case, which aligns with and confirms the previous theoretical studies given in Refs. [24, 25]. It is important to note that during the QR BECs from the surface, when approximately half of the condensate has been reflected, a superposition of the incident and reflected waves is formed. This causes periodic modulation in the density profile [see figure 3 during collision ($t = 41$ ms)]. Due to the strong interatomic potential energy in BEC C compared to their collision kinetic energy E_k, the high density at the peak of the standing wave causes atoms to be pushed out perpendicular to the x-direction, thereby transferring momentum to the y-direction. This results in the formation of significantly disturbed solitons until after reflection due to dynamical excitation at low v_x. The disturbed soliton formation indicates atomic cloud fragmentation in the QR, which appears more controlled at higher velocities. Consequently, anomalous

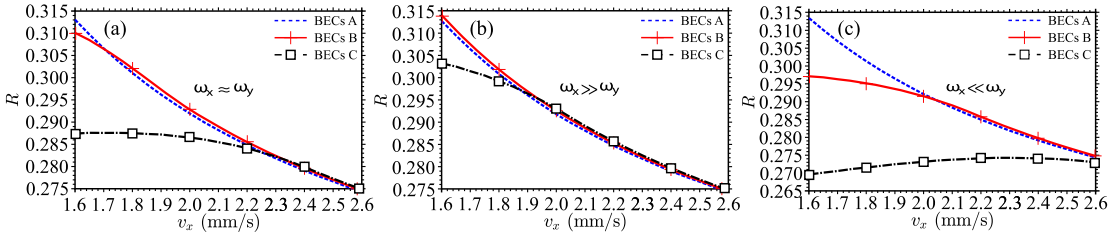

Figure 4. Reflection probability R versus incident velocity v_x of QR from the Si planar surface of interacting quasi-2D ^{23}Na BECs at $\theta = 90^\circ$ (normal incidence) under the influence of CP potential V_{CP} for cases: (a) isotropic BECs ($\omega_x \approx \omega_y$), (b) anisotropic BECs elongated in the y-direction ($\omega_x \gg \omega_y$), and (c) anisotropic BECs elongated in the x-direction ($\omega_x \ll \omega_y$). [Note: all simulations are conducted for three distinct interacting quasi-2D ^{23}Na BECs, i.e., BECs A-C, with the number of atoms N specified as given in table 1].

phenomena occur at low v_x but not at high v_x. This study in the 2D system provides new insights into how condensate fragmentation arises from dynamical excitation, leading to saturation effects, as next illustrated by the drop in R in figure 4. Unlike previous studies [24], our findings demonstrate fragmentation in the form of disturbed solitons, which we suspect to be quantum fluctuations of solitons and recommend for further exploration in the future.

Further consequences of the atomic cloud disruption at low v_x include saturation effects or anomalous reflectivity, which we subsequently demonstrate in figure 4. Before that, figure 3(a)-(c) also shows that the disruption of the atomic cloud at low v_x becomes more apparent when the anisotropic BEC C is elongated along the x-direction [Figure 3(c)] compared to the isotropic BEC C [figure 3(a)]. This is due to the larger atomic cloud size, which is valid and now shows the clear consequences of the BEC configuration we previously discussed in figure 2. Minimal disruption of the atomic cloud for all cases occurs when the anisotropic BEC C is elongated along the y-direction [figure 3(b)] due to the smaller atomic cloud size. Before the collision ($t = 0$ms), BEC C is in its ground state for all cases, as previously discussed in figure 2.

Figure 4 further illustrates the relationship between the reflection probability R and the incident velocity v_x of QR interacting quasi-2D ^{23}Na BECs at normal incidence, $\theta = 90^\circ$, respectively for isotropic and anisotropic 2D disk-shaped BECs (BECs A-C) under the influence of the V_{CP} potential. Figure 4(a) shows that isotropic 2D disk-shaped BECs experience a decrease in reflection probability R with increasing interatomic interactions (or increasing N); the most significant decrease occurs for BECs C in this case. At the same time, stronger interatomic interactions appear to allow anomalous behavior of R at low v_x [figure 4(a)], where R is expected to increase with decreasing v_x for QR on solid surfaces [1]. Based on figure 4(a), the anomalous behavior of R in QR from the planar Si surface (under V_{CP}) is shown by BECs B at $v_x \in [1.6, 1.8]$ mm/s and BECs C at $v_x \in [1.6, 2.4]$ mm/s in this case. The phenomenon of the saturation effect in QR of ^{23}Na BECs found in this isotropic case appears to align with studies in Refs. [7, 24, 25].

In contrast to previous studies [24, 25], we have illustrated the QR of interacting quasi-2D ^{23}Na BECs elongated in the x- and y-directions (anisotropic) under the influence of V_{CP} at normal incidence ($\theta = 90^\circ$). After calculating the reflection probability R against the incident velocity v_x, it appears that the saturation effect or anomalous behavior of R in the low v_x regime is somewhat suppressed when all 2D disk-shaped BECs are elongated in the y-direction, as depicted in figure 4(b). Conversely, figure 4(c) depicts the more significant anomalous behavior of R when 2D disk-shaped BECs are elongated in the x-direction. This aligns with the BEC configurations we discussed earlier in figure 2, with clear consequences for atomic cloud disturbance in figure 3(b)-(c). Although quasi-2D anisotropic BECs elongated in the y-direction result in minimal saturation effects in the low v_x regime [figure 4(c)-(d)], the saturation effect is not completely eliminated. This is especially true for BECs C, given the substantial size of the atomic cloud [figure 2(f)], which still shows disturbances in the atomic cloud [figure 3(b)]. The saturation effect for BECs C occurs at $v_x \in [1.6, 2.0]$ mm/s as shown in figure 4(b). Effective control over the anomalous behavior of R in this configuration is demonstrated by BECs A and B [Figure 4(b)] due to the smaller atomic cloud size [figure 2]. Of course, the strong disturbance in the condensate atomic cloud along the x-direction increases and becomes very significant when the quasi-2D anisotropic BECs are set to elongate in the x-direction, as previously shown in figure 3(c) for QR of BECs C from the planar Si surface. In this third configuration, the saturation effect of BECs B and C appears more pronounced [Figure 4(c)] compared to previous QR studies [figure 4(a)-(b)]. For BECs B, the anomalous behavior of R is now observed at $v_x \in [1.6, 2.2]$ mm/s. Meanwhile, $v_x \in [1.6, 2.6]$ mm/s is the regime that shows the anomalous behavior of R for BECs C, as shown in figure 4(c). Based on QR simulation results at normal incidence, $\theta = 90^\circ$, we conclude that, in principle, the saturation effect can be manipulated by adjusting the configuration of anisotropic 2D disk-shaped BECs or, in technical terms, adjusting the trap frequency configuration. This is

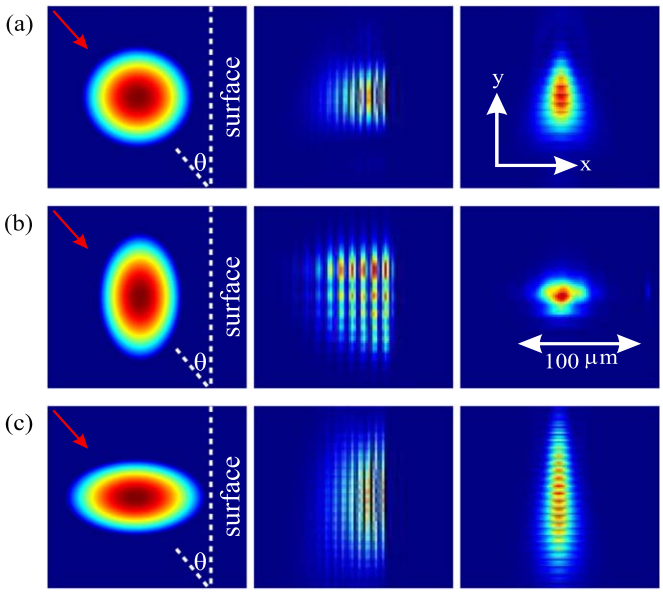

Figure 5. (dark red = high density) in the $x-y$ plane showing QR of isotropic (a), anisotropic elongated in y-direction (b), and anisotropic elongated in x-direction (c) ^{23}Na BECs C from a planar Si surface in angle of incidence $\theta = 15^0$ with incident speed $v_x = 1.0$ mm/s. From left to right represent BECs before ($t = 0$ ms), during ($t = 41$ ms), and after collision ($t = 63$ ms). The red arrows indicate the direction of BECs that undergo QR and the horizontal bar shows spatial scale.

highly relevant for cases involving relatively weaker interatomic interactions. Enhanced QR still requires strong interatomic interactions [11], and in this study, we propose QR based on the incident angle θ.

3.3. Quantum reflection based on angle of incidence

In this section, we present QR of interacting quasi-2D ^{23}Na BECs based on the variation of the incident angle, $\theta \in [15^\circ, 90^\circ]$. At normal incidence, $\theta = 90^\circ$, strong interatomic interactions (larger N) are known to cause significant disruption to the atomic cloud, leading to clear saturation effects or anomalous behavior of R at low velocities v_x [figures 3–4]. Therefore, as a first investigation, we examined QR of BEC C on a planar Si surface at an angle of incidence far from normal direction, $\theta = 15^\circ$. Figure 5(a)-(c) displays images of the 2D disk-shaped BEC C (isotropic and anisotropic) before ($t = 0$ ms), during ($t = 41$ ms), and after ($t = 63$ ms) collision with the planar Si surface at $\theta = 15^\circ$ and $v_x = 1.0$ mm/s.

The angle of incidence θ clearly plays a crucial role in controlling the disruption of the atomic cloud. Although disruption occurs in all configurations [figure 5(a)-(c)], it appears to be more controlled in the x-direction, where the condensate tends to concentrate towards the center of mass due to irregularities in that direction. For clearer comparison with QR at normal incidence ($\theta = 90^\circ$) [figure 3(a)-(c)], figure 5(a)-(c) shows that the disruption for angles far from normal incidence ($\theta = 15^\circ$) is relatively weaker along the x-direction. This is because θ induces a non-uniform atom cloud distribution at the minimum potential, leading to non-uniform collisions. Consequently, there is a release of non-uniform mean field energy of the BECs, and the incident kinetic energy becomes more dominant than the mean field energy, $E_g < E_k$ [further confirmed in figure 7(a)-(b)]. This results in the reduction of saturation effects, allowing the reflection probability to follow the curve of non-interacting BECs [25] or single-atom behavior [1], as further illustrated in figure 6. This phenomenon highlights the importance of the incident angle θ in regulating the dynamic properties associated with atomic collisions in the BEC system and provides deep insight into how geometry and initial conditions can affect the system's response to collisions, such as non-uniform atom-surface interactions. Therefore, this implies that considering QR of BECs based on the incident angle θ could be an alternative optimization for QR, leading us towards predictions made by quantum mechanics [1].

Figure 6(a1)-(c1) illustrates the relationship between the reflection probability R and the incident velocity v_x of QR interacting quasi-2D ^{23}Na BECs for the isotropic case based on the variation of the incident angle, $\theta \in [15^\circ, 90^\circ]$. Due to relatively weaker interatomic interactions, QR of BEC A does not exhibit anomalous behavior in the low v_x regime [Figure 6(a1)], consistent with our previous discussion [figure 4(a)]. In this scenario, the incident angle θ appears to enhance the reflection probability R. In figure 6(a1), the significant role of θ is not yet clearly evident, as indicated by the overlapping line graphs of R against v_x. The clear role of θ in enhancing R in the isotropic case is further demonstrated by BECs B and C [figure 6(b1)-(c1)], even restoring the saturation effect or anomalous behavior of R at low v_x for angles relatively far from normal direction, specifically

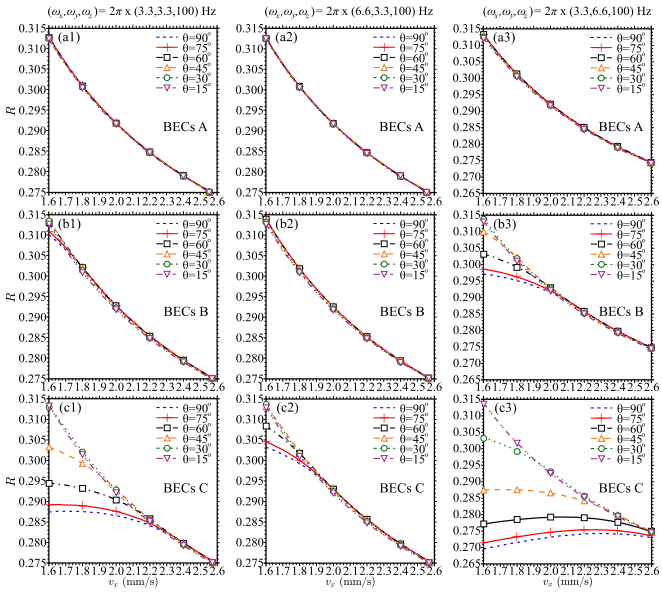

Figure 6. Reflection probability R versus incident velocity v_x for QR of interacting quasi-2D ^{23}Na BECs from a Si planar surface under the influence of CP potential V_{CP} for incidence angles: $\theta = 90°$, $\theta = 75°$, $\theta = 60°$, $\theta = 45°$, $\theta = 30°$, and $\theta = 15°$. (a1)-(c1) isotropic BECs ($\omega_x \approx \omega_y$), (a2)-(c2) anisotropic BECs elongated in the y-direction ($\omega_x \gg \omega_y$), and (a3)-(c3) anisotropic BECs elongated in the x-direction ($\omega_x \ll \omega_y$) [Note: all simulations were performed for three distinct interacting quasi-2D ^{23}Na BECs, i.e., BECs A-C, with the number of atoms N for each BECs specified as given in table 1].

when $\theta = 15°$ in this case. Figure 6(b1) shows the relationship between R and v_x from QR of BEC B in the isotropic case based on the incident angle θ under the influence of V_{CP}. As the incident angle varies, $\theta \in [15°, 90°]$, figure 6(b1) shows a more significant increase in R (with decreasing v_x) when QR of BEC B starts from an angle far from normal incidence ($\theta \to 15°$). In this situation, the saturation effect or anomalous behavior of R in the low v_x regime appears to be mitigated and even eliminated for smaller θ, specifically when $\theta = 15°$ in this case [figure 6(b1)]. Further control over the saturation effect or anomalous behavior of R at low v_x is then more clearly demonstrated by QR of BEC C [figure 6(c1)]. BEC C, as we understand, has a much larger atomic cloud size compared to the other two BECs under consideration [figure 2]. The incident angle θ then offers manipulation of the collision, uneven atom-surface interactions, which in turn results in controlled disruption in the condensate atomic cloud in the low v_x regime, as previously shown in figure 5(a) for isotropic QR of BEC C from a planar Si surface at $\theta = 15°$. Therefore, it is important to note that the saturation effect or anomalous behavior of R in QR from quasi-2D BECs with very strong interatomic interactions can be optimally mitigated and even eliminated by the incident angle, as in the case of QR of BEC C at $\theta = 15°$ shown in this study [figure 6(c1)].

In this study, we also show the influence of the incident angle θ on QR of interacting quasi-2D ^{23}Na BECs in the anisotropic case under the actual potential from a planar Si surface modeled by V_{CP}, as shown in figure 6(a2)-(c2) and figure 6(a3)-(c3). Figure 6(a2)-(c2) illustrates the relationship between the reflection probability R and the incident velocity v_x of the 2D disk-shaped BEC elongated in the y-direction. At $\theta = 90°$, all phenomena return to normal incidence [as previously discussed in figure 4(b)]. At the same time, figure 6(a2)-(c2) shows that the saturation effect or anomalous behavior of R in the low v_x regime can be mitigated and even eliminated, specifically under conditions of incident angles relatively far from normal incidence, $\theta = 15°$ in this case. Now, the role of the incident angle θ becomes more evident, offering better control over the saturation effect at low v_x, even more so than has been achieved by configuring the 2D disk-shaped BEC elongated in the y-direction at normal incidence [see the comparison of simulation results provided in figure 4(b) and figure 6(a2)-(c2)]. Furthermore, when we arrange the configuration of the 2D disk-shaped BECs elongated in the x-direction, disruption effects on the condensate atom cloud along the x-direction become more significant [see again figure 3(c)], and the angle of incidence ($\theta = 15°$) can still control these disruptions figure 5(c)], which in turn provides optimal control over saturation effects. Anomalous behavior of R in the low v_x regime is completely overcome and disappears in this third configuration, as shown in figure 6(a3)-(c3). Based on our findings in this study, we assess that by considering QR BECs based on the angle of incidence θ, we can achieve good agreement with what has been predicted by quantum mechanics in single-atom theory, where the reflection probability R monotonically increases with decreasing incident velocity v_x [1]. In this study, the angle of incidence θ is found to manipulate atom-surface interactions, leading to control of saturation effects. Based on our calculations, we can enhance QR ^{23}Na BECs with strong interatomic interactions (such as BECs C in this study) based on an angle of

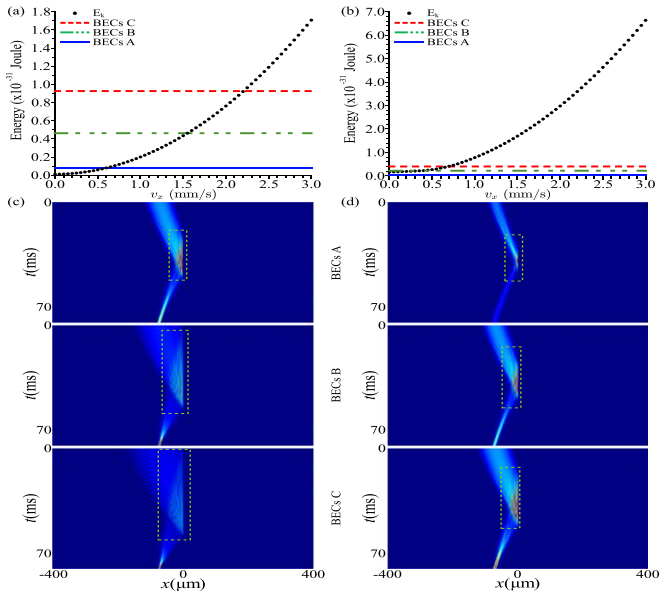

Figure 7. Incident kinetic energy E_k of ^{23}Na BEC versus incident velocity v_x (black dotted line) and incident mean-field energy for BECs A, B, and C (respectively marked by blue, green, and red horizontal lines) at: (a) $\theta = 90^\circ$ and (b) $\theta = 15^\circ$. Density profiles of the matter wave condensates along the x-direction during QR, successively from top to bottom for BECs A, B, and C at: (c) $\theta = 90^\circ$ and (d) $\theta = 15^\circ$.

incidence around 8.68% for isotropic BECs, 3.30% for anisotropic BECs elongated in the y-direction, and 17.10% for anisotropic BECs elongated in the x-direction, respectively calculated based on the maximum increase in reflection probability achieved by angles of incidence from normal incidence. Thus, if the latest experiments have been able to achieve a QR enhancement of 70% at normal incidence [11], then following the significant figures offered by the angles of incidence above could lead us to the next maximal achievement. Therefore, we propose new experiments related to QR BECs based on the angle of incidence θ in the future, especially to realize its practical applications.

3.4. Mean field energy, incident kinetic energy, and spread of matter-wave condensate

To conclude the discussion, we investigate the relationship between the incident kinetic energy E_k and the mean-field energy E_g during QR of quasi-2D ^{23}Na BECs. These quantities are derived from the Gross–Pitaevskii equation (GPE) as defined in section 2.3. The kinetic energy of the condensate is associated with the spatial variation of the wavefunction, which corresponds to the Laplacian term in the GPE. The total kinetic energy is given by [32]:

$$E_k = \int \frac{\hbar^2}{2m} |\nabla \psi(\mathbf{r})|^2 d\mathbf{r}, \tag{3}$$

where $\psi(\mathbf{r})$ is the condensate's wavefunction, and $\nabla \psi(\mathbf{r})$ is the gradient of the wavefunction. This term reflects the energy resulting from the spatial gradients of the wavefunction. Meanwhile, The mean-field energy arises from the interatomic interactions, represented by the nonlinear term in the GPE. The total mean-field energy is given by [32]:

$$E_g = \int g|\psi(\mathbf{r})|^4 d\mathbf{r}, \tag{4}$$

where $g = \frac{4\pi\hbar^2 a}{m}$ is the interaction strength, and a is the s-wave scattering length as defined in section 2.3. This term captures the energy due to the interactions between atoms in the condensate.

These two energies, E_k and E_g, determine the energy profile of the system and influence the behavior of the condensate during QR. As shown in figure 7, the relative magnitudes of these energies affect the reflection dynamics of the BEC. At low velocities, the mean-field energy E_g dominates, leading to saturation effects, while at higher velocities, the kinetic energy E_k becomes more significant. Figure 7(a) illustrates the relationship between the incident kinetic energy E_k (black dotted line) and the mean-field energy E_g for BECs A, B, and C during QR at $\theta = 90^\circ$. The saturation effects at normal incidence can be attributed to the dominance of E_g over E_k in the low velocity range, as observed in the velocity range $v_x \in [0.0, 2.4]$mm/s. This behavior is consistent with the results shown in figure 4, where saturation effects are more pronounced in BEC C due to stronger

interatomic interactions. In contrast, when the angle of incidence is set to $\theta = 15^{\circ}$, as shown in figure 7(b), the kinetic energy E_k dominates for all BECs in the low velocity range, as the angle of incidence alters the condensate's spatial distribution. This shift in the dominance of E_k over E_g reduces the saturation effects in the low v_x regime, as seen in figure 4.

The density profiles of matter-wave condensates along the x-direction during QR are depicted in figure 7(c)-(d). These profiles qualitatively validate our findings, showing significant spreading of the matter-wave density during atom-surface interactions. Notably, BEC C exhibits the most pronounced spreading due to stronger interatomic interactions (larger N) and dominant E_g. This supports our conclusion that saturation effects arise primarily from E_g, and their mitigation is effectively controlled by the angle of incidence θ. Our results align with earlier studies on the dominance of mean-field energy in QR-induced saturation effects [24, 25]. Furthermore, we highlight the novel observation of condensate matter-wave density spreading during QR, which has not been reported in prior works. This qualitative evidence strengthens the interpretation that θ offers a robust mechanism to control saturation effects, particularly in strongly interacting systems.

4. Summary

We have explored the phenomenon of QR interacting quasi-2D ^{23}Na BECs from the planar Si surface based on the angle of incidence θ, focusing on three distinct BECs with different numbers of atoms N, labeled as BECs A-C. QR interacting quasi-2D ^{23}Na BECs were modeled using CP potential as a planar Si surface model. Both isotropic and anisotropic 2D disk-shaped BECs were considered. We found that the incidence angle θ plays a crucial role in inducing non-uniform atom-surface interactions, which in turn minimizes and even eliminates the anomalous reflectivity at low incident velocities, known as the saturation effect. These findings provide new insights into enhancing the reflection probability R in the study of QR BECs from solid surfaces, which has not been maximally achieved due to saturation effects since the first experiments [11]. Achieving a high reflection probability R could lead to the construction of new atomic optical devices, such as mirrors and cavities, without requiring magnetic or optical fields [41–45]. Additionally, QR BECs have practical potential as a universal mechanism for confining ultracold atoms [20–23]. Therefore, we propose new experiments related to QR BECs based on the angle of incidence θ in the future.

In this study, we found that the saturation effect can be minimized by adjusting the trap frequency so that the 2D disk-shaped BECs become anisotropic, elongating perpendicular to the reflection direction (the y-direction in our case). However, this approach cannot completely eliminate the saturation effect in the low incident velocity regime. In contrast, the angle of incidence θ can optimally overcome the saturation effect in this regime, even when severe disruptions occur in the condensate atom cloud with a 2D disk-shaped BEC elongating in the x-direction or parallel to the reflection direction. Therefore, the angle of incidence is crucial in optimizing QR. Besides controlling the saturation effect to enhance the reflection probability R, this study also shows that the saturation effect in QR BECs occurs due to the dominance of mean-field energy over incident kinetic energy, clarifying previous interpretations. Our findings are relevant to the broader community, especially those studying Bose–Einstein condensates and their applications.

Acknowledgments

The authors would like to acknowledge the support from the Fundamental Research Grant Scheme (FRGS) under the grant number FRGS/1/2019/STG02/UNIMAP/02/9 from the Ministry of Education Malaysia. This work was supported financially by FRGS.

Data availability statement

All data that support the findings of this study are included within the article (and any supplementary files).

ORCID iDs

H A Musyayyadah https://orcid.org/0009-0007-7431-7413
M N A Halif https://orcid.org/0000-0001-9499-8139
A Ripai https://orcid.org/0000-0002-9453-6142
Z Abdullah https://orcid.org/0000-0002-8052-0836

References

[1] Shimizu F 2001 *Phys. Rev. Lett.* **86** 987
[2] Friedrich H, Côté R and Trost J 1997 *Phys. Rev.* A **56** 1781
[3] Friedrich H, Jacoby G and Meister C G 2002 *Phys. Rev.* A **65** 032902
[4] Shimizu F and Fujita J I 2002 *J. Phys. Soc. Japan* **71** 5–8
[5] Shimizu F and Fujita J I 2002 *Phys. Rev. Lett.* **88** 123201
[6] Druzhinina V and DeKieviet M 2003 *Phys. Rev. Lett.* **91** 193202
[7] Pasquini T A, Shin Y, Sanner C, Saba M, Schirotzek A, Pritchard D E and Ketterle W 2004 *Phys. Rev. Lett.* **93** 223201
[8] Nayak V U, Edwards D O and Masuhara N 1983 *Phys. Rev. Lett.* **50** 990
[9] Yu I A, Doyle J M, Sandberg J C, Cesar C L, Kleppner D and Greytak T J 1993 *Phys. Rev. Lett.* **71** 1589–92
[10] Wang D M, Xing J C, Du R, Xiong B and Yang T 2021 *Chin. Phys.* B **30** 120303
[11] Pasquini T A, Saba M, Jo G B, Shin Y, Ketterle W, Pritchard D E, Savas T A and Mulders N 2006 *Phys. Rev. Lett.* **97** 093201
[12] Scott R G, Hutchinson D A W and Gardiner C W 2006 *Phys. Rev.* A **74** 053605
[13] Scott R G, Gardiner C W and Hutchinson D A W 2007 *Laser Phys.* **17** 527–32
[14] Cornish S L, Parker N G, Martin A M, Judd T E, Scott R G, Fromhold T M and Adams C S 2009 *Physica D: Nonlinear Phenomena* **238** 1299–305
[15] Judd T, Henning A, Hardwick D, Scott R, Balanov A, Wilkinson P, Fowler D, Martin A and Fromhold T 2007 *Prog. Theor. Phys. Suppl.* **166** 169–78
[16] Judd T E, Scott R G, Martin A M, Kaczmarek B and Fromhold T M 2011 *New J. Phys.* **13** 083020
[17] Marchant A L, Billam T P, Yu M M H, Rakonjac A, Helm J L, Polo J, Weiss C, Gardiner S A and Cornish S L 2016 *Phys. Rev.* A **93** 021604
[18] Cheng Q L, Bai W K, Zhang Y Z, Xiong B and Yang T 2018 *Laser Phys.* **29** 015501
[19] Musyayyadah H A, Ripai A and Halif M N A 2023 *International Journal of Nanoelectronics and Materials* **16** 461–8
[20] Madronero J and Friedrich H 2007 *Phys. Rev.* A **75** 022902
[21] Doyle J M, Sandberg J C, Ite A Y, Cesar C L, Kleppner D and Greytak T J 1991 *Phys. Rev. Lett.* **67** 603
[22] Jurisch A and Friedrich H 2006 *Phys. Lett.* A **349** 230–5
[23] Jurisch A and Rost J M 2008 *Phys. Rev.* A **77** 043603
[24] Scott R G, Martin A M, Fromhold T M and Sheard F W 2005 *Phys. Rev. Lett.* **95** 073201
[25] Halif M N A 2012 *Quantum Reflection of Bose-Einstein Condensates from Dielectric Surfaces Ph.D. thesis* (University of Nottingham)
[26] Segev B, Côté R and Raizen M G 1997 *Phys. Rev.* A **56** R3350
[27] de Carvalho J X, Hussein M S and Li W 2008 *Phys. Rev.* A **78** 032906
[28] Min L and Ming-Sheng Z 2008 *Chin. Phys. Lett.* **25** 3154
[29] Marchant A L, Billam T P, Wiles T P, Yu M M H, Gardiner S A and Cornish S L 2013 *Nat. Commun.* **4** 1865
[30] Lee C and Brand J 2005 *Europhys. Lett.* **73** 321
[31] Benseghir A, Wan Abdullah W A T, Baizakov B B and Abdullaev F Kh 2014 *Phys. Rev.* A **90** 023607
[32] Pethick C J and Smith H 2008 *Bose–Einstein condensation in dilute gases* (Cambridge university press)
[33] Pitaevskii L and Stringari S 2016 *Bose-Einstein condensation and superfluidity* 164 (Oxford University Press)
[34] Casimir H B G and Polder D 1948 *Phys. Rev.* **73** 360
[35] Adhikari S K 2000 *Phys. Lett.* A **265** 91–6
[36] Adhikari S K 2000 *Phys. Rev.* E **62** 2937
[37] Press W H 2007 *Numerical recipes 3rd edition: The art of scientific computing* (Cambridge university press)
[38] Scott R G, Martin A M, Fromhold T M, Bujkiewicz S, Sheard F W and Leadbeater M 2003 *Phys. Rev. Lett.* **90** 110404
[39] Scott R G, Martin A M, Bujkiewicz S, Fromhold T M, Malossi N, Morsch O, Cristiani M and Arimondo E 2004 *Phys. Rev.* A **69** 033605
[40] Kuopanportti P, Huhtamäki J A M and Möttönen M 2011 *Phys. Rev.* A **83** 011603
[41] Hinds E A and Hughes I G 1999 *J. Phys. D: Appl. Phys.* **32** R119
[42] Noh H R and Jhe W 2002 *Phys. Rep.* **372** 269–317
[43] Mohapatra A K, Chaudhuri S, Roy S and Unnikrishnan C S 2007 *Eur. Phys. J.* D **42** 287–98
[44] Cronin A D, Schmiedmayer J and Pritchard D E 2009 *Rev. Mod. Phys.* **81** 1051
[45] Heine N, Matthias J, Sahelgozin M, Herr W, Abend S, Timmen L, Müller J and Rasel E M 2020 *Eur. Phys. J.* D **74** 18